Research Article Vol. 34, No. 10 / 18 May 2026 / Optics Express 18620
Optics EXPRESS

# Low-voltage silicon photonics modulator with CMOS-compatible driving for compact quantum key distribution transmitters

ZHAO-YUAN CHEN,[1,2,3,4,†] YU-ANG WANG,[1,2,3,†] JIANG-KAI YU,[1,2,3] WEN-SHUAI TANG,[1,2,3] YIN-RAN LI,[1,2,3] SHUO LI,[4] XIAN-CHANG DU,[5] REN-DE LIU,[5] JI-GANG REN,[1,2,3] JUAN YIN,[1,2,3] YAN-FEI LIU,[4] HAO ZHENG,[4] YANG LI,[1,2,3,6] SHENG-KAI LIAO,[1,2,3,7] AND CHENG-ZHI PENG[1,2,3]

[1]*Hefei National Research Center for Physical Sciences at the Microscale and School of Physical Sciences, University of Science and Technology of China, Hefei 230026, China*
[2]*Shanghai Research Center for Quantum Science and CAS Center for Excellence in Quantum Information and Quantum Physics, University of Science and Technology of China, Shanghai 201315, China*
[3]*Hefei National Laboratory, University of Science and Technology of China, Hefei 230088, China*
[4]*Xi'an Research Institute of High Technology, Xi'an 710025, China*
[5]*QuantumCTek Corporation Limited, Hefei, Anhui 230088, China*
[6]*liyang9@ustc.edu.cn*
[7]*skliao@ustc.edu.cn*
[†]These authors contributed equally to this work.

**Abstract:** Most quantum key distribution (QKD) silicon photonic chips rely on carrier depletion modulators (CDM), which typically require driving voltages beyond 5 V due to their limited modulation efficiency. In this work, we employ a carrier injection modulator (CIM) for quantum bit encoding, which offers a fundamentally higher modulation efficiency and thus a path to significantly lower operating voltages. Through structural optimization, the CIM achieves a half-wave voltage of 1.1 V (DC) and 1.28 V (at 100 MHz), with a modulation depth exceeding 24 dB under both conditions. Successful demonstrations of intensity state preparation as well as polarization state modulation were also conducted. These results confirm the suitability of the CIM for compact and energy-efficient QKD transmitters operating at CMOS-compatible voltages.

© 2026 Optica Publishing Group under the terms of the Optica Open Access Publishing Agreement

## 1. Introduction

Quantum key distribution (QKD), as a potential method to resist the information security risk brought by quantum computing [1,2], has been widely researched and developed [3–9]. After witnessing the triumph that quantum satellite and network accomplished [10–17], quantum communication industry becomes a rising star and attracts much attention of commercial community. As an quantum shield in the future information security, quantum communication technology has great commercial value, and many organizations are increasing their investment in this field. Recent research has also gradually tilted towards the direction of practical application.

Different from laboratory experiments, real world applications face more complicated environments. High stability, compact size, low power consumption and cost are some of key targets for industry development. Fortunately, these features are also demanded by classical optical communication (COC) industry. COC successfully opened up its industrial territory by leveraging the photonics integrated chip (PIC) technology. Quantum communication can follow the route of COC and realize the transformation from experimental research to application development. In 2017, Sibson et al. proposed a chip based quantum communication system

#595583 https://doi.org/10.1364/OE.595583
Journal © 2026 Received 3 Mar 2026; revised 2 May 2026; accepted 5 May 2026; published 12 May 2026

Optics EXPRESS

using an indium phosphide (InP) transmitter chip and a silicon oxynitride receiver chip [18]. This work shows the feasibility of miniaturization of QKD module with the help of integrated photonics technology, and sparks a wave of research on integrated QKD transmitter [19–23].

While significant progress has been made in integrated QKD photonics modules, researchers have also embarked on the study of integrated QKD systems [24,25]. However, QKD electronics driver design has much more differences compared with COC. Quantum bits encoding demands precise phase control and deep phase modulation, which leads to a requirement of low noise and high voltage driving signal [26]. In Ref. [18], the half-wave voltage (HWV) of InP chip is up to 10 V. Refs. [20,27,28] use silicon photonics modulator, and its HWV is about 5 to 6 V. Since the maximum modulation phase is $\frac{3}{2}\pi$, the maximum voltage actually used in these work will be 1.5 times the HWV. By extending the modulator length, Zhu et al. achieved a silicon photonics chip with HWV of 3.27 V [25]. However, the maximum required voltage is still around 5 V. Hence they add radio frequency (RF) amplifiers to the system, which has huge power consumption and increases the design difficulty of compact module. In 2023, Sax et al. proposed a high-speed integrated QKD system using carrier injection modulators (CIM) [29]. They use a cascade of three modulators and equalization schemes in the electronic driver design to overcome the bandwidth limitation and achieve high-speed QKD. This solution reduces the driving voltage requirement of the modulator, which can be met by a voltage of 3 V. But at the same time, more channel driver signals are needed, and the complexity of driver circuit design is not reduced.

Inspired by this CIM scheme, we propose its optimized use in a QKD transmitter. Owing to the pursuit of high modulation rate (tens of Gbits/s) and relatively low modulation depth (about 10 dB) in COC, the carrier depletion modulator (CDM) scheme is widely adopted due to its high bandwidth (over 20 GHz). This route is also inherited by QKD transmitter design, with most silicon photonics chips employing CDM [20,25,27,28,30–32]. However, quantum states preparation in QKD requires high extinction ratio that is typically 20 to 30 dB. Low modulation efficiency of the depletion effect is the key limitation of reducing driver voltage demands. CIM can compensate for this deficiency through its high electro-optic effect. Although traditionally considered low-speed modulators (operation speed beneath 5 Gbits/s) due to long carrier recombination lifetime [33], the clock rate of most practical QKD systems ranges from hundreds of MHz to a few GHz, with the state-of-the-art reaching 3.3 GHz [34]. Consequently, the clock rate of mainstream QKD systems can be readily addressed by CIM. Therefore, in this work we employ a CIM design to achieve CMOS-compatible driving voltages at hundred-MHz repetition rates, alongside high modulation depth and sufficient speed, for compact QKD transmitters.

## 2. Design principle and simulation results

As illustrated in Fig. 1(a), we use an Mach-Zehnder interferometer (MZI) to realize intensity modulation. Each arm of the MZI consists of a CIM and a thermal phase shifter (PS). Figure 1(b) is the cross section of the CIM, which is a rib waveguide structure with different doping type on two side. The rib width is 500 nm, and a PN junction diode is formed at this region. Since CIM operates under forward bias condition, we next assume the a positive voltage signal is applied in the P region and analyze the electronic and optical dynamic process of the diode.

As depicted in Fig. 2(a), $V_0$ is applied to the CIM at moment $t_1$. $V_0$ is higher than the diode threshold voltage $V_t$. Hence, under the influence of an applied electric field $\mathscr{E}$, the PN junction forms a forward current $I$:

$$I = \iint_A J_e + J_h dS, \tag{1}$$

$$J_e = qN_e\mu_e\mathscr{E} + qD_e\frac{\partial N_e}{\partial x}, \tag{2}$$

Optics EXPRESS

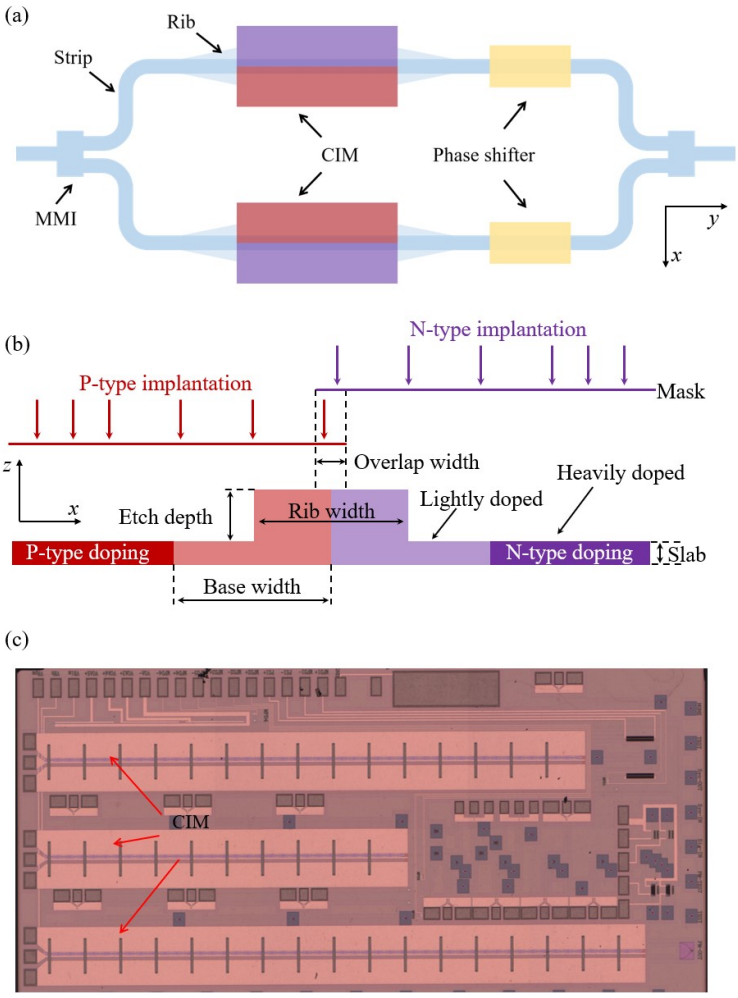



**Fig. 1.** Modulator structure diagram. (a) The intensity modulator consists of a symmetrical MZI formed by strip waveguides and a multi-mode interferomter (MMI) coupler, with a CIM and a phase shifter integrated on each arms. (b) The cross section profile of the CIM. The waveguide is fabricated by etching a 220 nm-thick silicon layer, with a rib region etch depth of 150 nm. The rib waveguide region is lightly doped, while the slab is heavily doped. The overlap width refers to the overlapping region of the P and N implantation masks, while the base width denotes the distance between the waveguide center and the heavily doped areas. (c) The microscope image of the fabricated MZI.

$$J_h = qN_h\mu_h\mathscr{E} - qD_h\frac{\partial N_h}{\partial x}, \tag{3}$$

where the subscript $e$ and $h$ denote the electron and hole respectively, $q$ is the elementary charge, $N$ is the carrier density, $\mu$ is the carrier mobility, $D$ is the diffusion coefficient. The variation of the current $I$ is shown in Fig. 2(b).

We denote the total current $I$ as two part: $I = I_c + I_F$, where $I_c$ is the charging current and $I_F$ is diode forward conduction current. This charging process involves two stages. One is charging up the depletion-layer capacitor. The depletion-layer capacitance is typically on the order of fF/μm$^2$, and the voltage swing is typically about 1 V. The diode carries a current density of mA/μm$^2$, then the depletion-layer charging time is on the order of ps, which is very short and leads to the

Optics EXPRESS

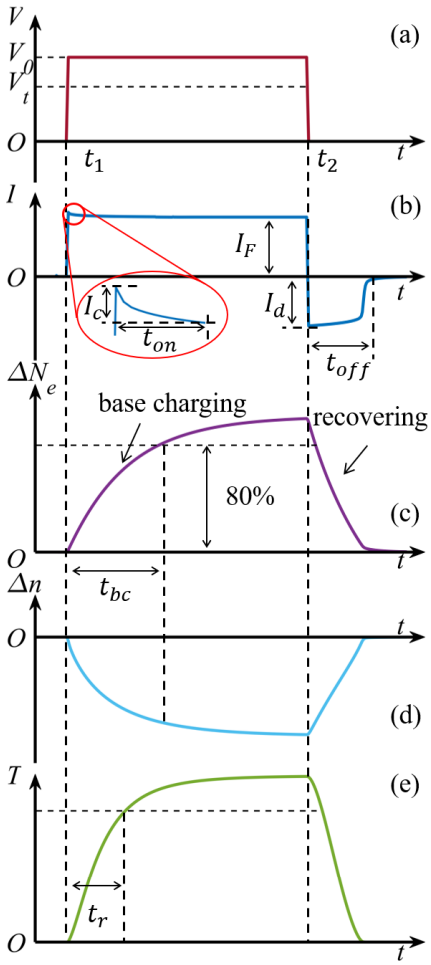



**Fig. 2.** CIM transient characteristics schematic. (a) A voltage signal is applied on the modulator at $t_1$ and removed at $t_2$. (b) The current response of the modulator under applied voltage. (c), (d), and (e) are the electron density, refractive index, and optical transmission variation curves, respectively.

rapid decrease of $I_c$. Another is filling up the P- and N-base with excess minority carries. For a narrow-base diode, the P-base charging time equals to the base-transit time $t_B$ [35]:

$$t_B = \frac{W^2}{2D_e}, \tag{4}$$

where $W$ is the base width. Though $t_B$ is much longer than the depletion-layer charging time, the charging current $I_c$ is very small, and $I_{tot}$ tends to stabilize at $I_F$. Therefore, when the depletion-layer charging is complete, the diode can be considered to be turned on from an electronic perspective.

But from an optical point of view, this process does not fully enter the steady state. According to continuity equations, the carrier density change can be expresses as:

$$\frac{\partial N_e}{\partial t} = \frac{1}{q}\frac{\partial J_e}{\partial x} - R_e + G_e, \tag{5}$$

Optics EXPRESS

$$\frac{\partial N_h}{\partial t} = -\frac{1}{q}\frac{\partial J_h}{\partial x} - R_h + G_h, \tag{6}$$

where $R$ and $G$ are recombination and generation rates. Since free carriers are still being injected into the base region, as shown in Fig. 2(c), the optical refractive index and loss are varying according to the plasma dispersion effect [36]:

$$\Delta n = -[8.8 \times 10^{-22} \times \Delta N_e + 8.5 \times 10^{-18} \times (\Delta N_h)^{0.8}] \tag{7}$$

$$\Delta \alpha = 8.5 \times 10^{-18} \times \Delta N_e + 6.0 \times 10^{-18} \times (\Delta N_h), \tag{8}$$

where $\Delta n$ and $\Delta \alpha$ are changes in refractive index and loss resulting from changes in the free electron $\Delta N_e$ and hole $\Delta N_h$ concentrations. The time from when $\Delta N_e$ begins to change until it reaches 80% of its maximum value is defined as the base charging time $t_{bc}$, and the same principle applies to other rise (or fall) time definitions. If an optical signal was modulated in this process, the transmission coefficient $T$ can be expressed as:

$$T = cos^2(\pi \Delta n \frac{L}{\lambda_0}), \tag{9}$$

where $L$ is the modulator length, and $\lambda_0$ is wavelength. While the transmission coefficient rise time $t_r$ depends on $t_{bc}$, it is not solely governed by it. Increasing the modulator length can also further enhance the rise time performance.

The turn-off process follows the same kinetic theory. When the voltage $V$ returns to zero at time $t_2$, a backward discharging current $I_d$ is formed, and takes a time of $t_{off}$ to drain off all the excess carriers. Since $I_d$ is larger than $I_c$, the carrier density recovering is much faster than charging, resulting a shorter transmission coefficient fall time. To conclude, the electro-optic response behavior of the CIM exhibits strong correlations with doping concentration profiles, spatial distribution of doped regions, and device geometric parameters. Consequently, our subsequent device design and simulation will focus on systematic optimization of these critical parameters.

In this work, the thickness of the silicon layer is fixed at 220 nm, and the rib etch depth is 130 nm. Several fixed doping levels are provided in the process. Low-concentration doping (approximately $10^{17}$ cm$^{-3}$) is applied in the rib waveguide region to reduce optical loss, while high-concentration doping (approximately $10^{18}$ cm$^{-3}$) is used in the slab region to lower electrical resistance. A series of simulations were conducted by varying the base width and overlap width configurations, with quantitative evaluation of key performance metrics including the half-wave voltage length $V_\pi L$, optical loss, and switching time $t_{off}$. The corresponding results are plotted in Fig. 3. The simulation results reveal a clear trade-off: the upper-right region exhibits low $V_\pi L$ and loss but is associated with a high $t_{off}$, whereas the lower-left region favors faster switching speed at the expense of modulation efficiency. After carefully balancing these trade-offs, the parameters indicated by the white dot in the figure were selected as the optimized configuration. This choice achieves relatively faster switching speed while maintaining a lower $V_\pi L$.

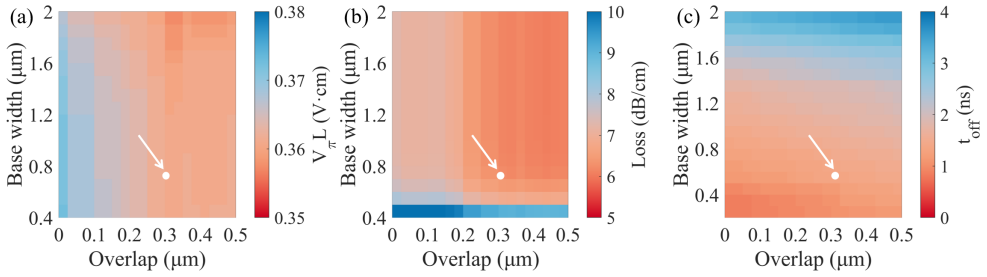



**Fig. 3.** Simulation results under different overlap and base width. (a) Half-wave voltage length $V_\pi L$. (b) Optical loss. (c) Diode turn-off time $t_{off}$.

Optics EXPRESS

## 3. Device fabrication and performance characterization

The optimized geometric configuration of the CIM was determined to be: a base width of 0.7 μm, an overlap width of 0.305 μm, and a total device length of 4.5 mm. The devices were fabricated by a commercial silicon photonics foundry CompoundTek through a multi-project wafer process [37]. Figure 1 shows the microscope image of the fabricated MZI.

We first conducted static characterization of the device to evaluate the CIM's electro-optic modulation efficiency and depth. A 1550.12 nm DFB laser diode, working at continuous wave mode, was used as optical source and input into the MZI. We applied different DC voltages on the PS and CIM, and recorded the output optical power. The photonic chip is mounted on a thermoelectric cooler (TEC) with active temperature control to ensure system stability, as both the waveguide refractive index (via the thermo-optic effect) and phase shifters (including the CIM) are sensitive to temperature variations. The experimental results are shown in Fig. 4. When a 4.4 V voltage is applied to the PS, the MZI reaches destructive interference state, and the maximum extinction ratio is about 24.1 dB. When the PS voltage is set to 4.4 V, the CIM achieves its optimized modulation performance with a maximum extinction ratio of 24.2 dB and a required voltage of only 1.1 V. Therefore, the measured $V_\pi L$ is about 0.5 V·cm, which is in reasonable agreement with the simulated value of 0.36 V·cm. The slight discrepancy is likely attributable to minor deviations in the fabricated device geometry or doping profiles from the ideal simulated structure.

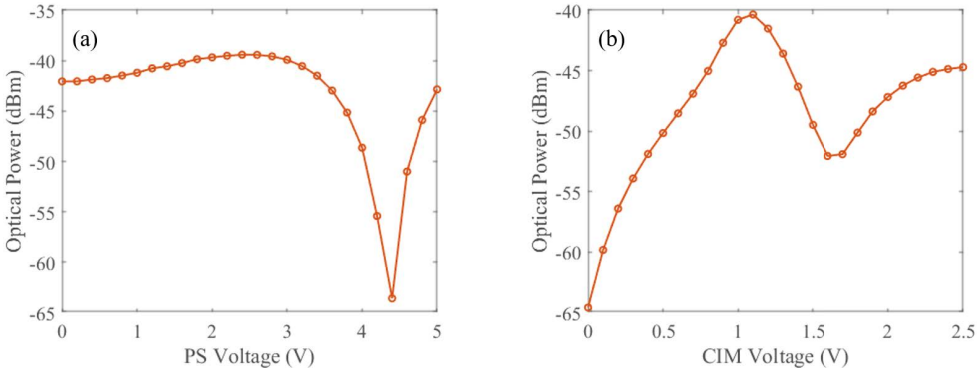



**Fig. 4.** Static experimental result. (a) Variation of output optical power under different PS voltages. (b) CIM modulation characteristic curves with different PS voltages. The measured half-wave voltage is 1.1 V, corresponding to a $V_\pi L$ of 0.5 V·cm, which is relatively close to the simulation result of 0.36 V·cm.

Then, we measured the electro-optic bandwidth and the optical modulation eye diagram of the device. The measured $S_{21}$ parameter of the device is shown in Fig. 5. At a bias voltage of 0.5 V, the 3-dB bandwidth of the CIM device is 6.85 GHz. As the bias voltage increases, the device bandwidth gradually decreases. When the bias voltage is 0.8 V, the bandwidth drops to 1.67 GHz. When the bias voltage reaches 1 V, the bandwidth further decreases to 0.34 GHz. We applied an AC voltage signal with $V_{pp}$ of 1 V on the CIM. Figure 6 displays eye diagrams measured at six distinct modulation frequencies. The optical output waveform exhibits excellent agreement with the simulated results in Fig. 2(e) (Note: The photoreceiver (Newport, model 1544-B) used to detect the optical signal featured negative coefficient gain, thus the measured waveform should be inverted about the x-axis for direct comparison). As the frequency increases, the vertical and horizontal openings of the eye diagram gradually decrease, mainly due to the increasingly slower rising and falling edges. At 1 GHz, significant eye closure becomes evident. However, the rise

Optics EXPRESS

time remains within 400 ps. This behavior indicates that the CIM device's bandwidth is about 1 GHz, which aligns well with the simulated switching speed on the order of ns.

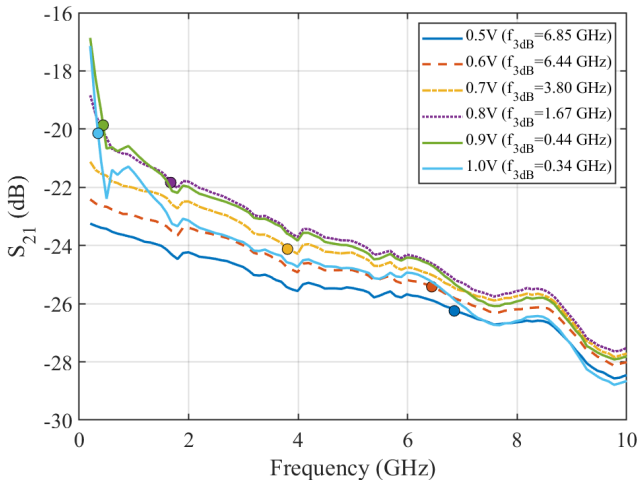



**Fig. 5.** $S_{21}$ curves under different bias voltages. When the bias voltage is below 0.9 V, the device bandwidth can reach above 1 GHz. When the bias voltage exceeds 0.9 V, the device bandwidth drops below 1 GHz. This is consistent with the simulated $t_{off}$ of 1.5 ns.

To validate our modulator's performance in QKD applications, we first evaluated its capability in polarization encoding using the same CIM design with the same architecture in Ref. [25]. Notably, the polarization modulation module was fabricated on the same chip using the same process. We drive the DFB laser diode in gain-switch mode to generate week coherent pulses. As shown in Fig. 7(a), a 100 MHz pseudo-random bit sequence (1.28 V amplitude), generated by a Keysight 81134A pattern generator, was used to modulate two polarization states. After attenuation, the modulated pulses were routed through a polarization decoding module before being coupled into the superconducting nanowire single-photon detector (SNSPD). The SNSPD's P channel and N channel, which represent the two detection channels aligned with the P state and N state respectively, were then read out and counted according to a synchronization signal. The photon distribution histogram demonstrates clear separation between the orthogonal polarization states, with an average PN extinction ratio of 27.5dB within the 192 ps gating window.

We further conducted decoy-state preparation experiments to assess the modulator's performance in intensity encoding. Similarly, we adjusted the PS bias voltage to make the MZI destructive interfere, and applied an 100 MHz pseudo random bit sequence signal (1.28 V amplitude) on the CIM to prepare signal and vacuum states. The photon counting distribution histogram is shown in Fig. 7(b). The blue squares and red circles represent vacuum and signal states respectively. Within the 192 ps gating window, the signal and decoy states exhibit an average extinction ratio of 24.4 dB.

Additionally, we performed experiments at a higher repetition rate of 1 GHz to verify the modulator's performance under more demanding conditions. Using a 2 V amplitude signal, the polarization encoding maintained an extinction ratio over 21 dB, while the decoy-state preparation achieved an extinction ratio exceeding 24 dB. These results validate the consistent performance of the modulator across different operating conditions.

Optics EXPRESS

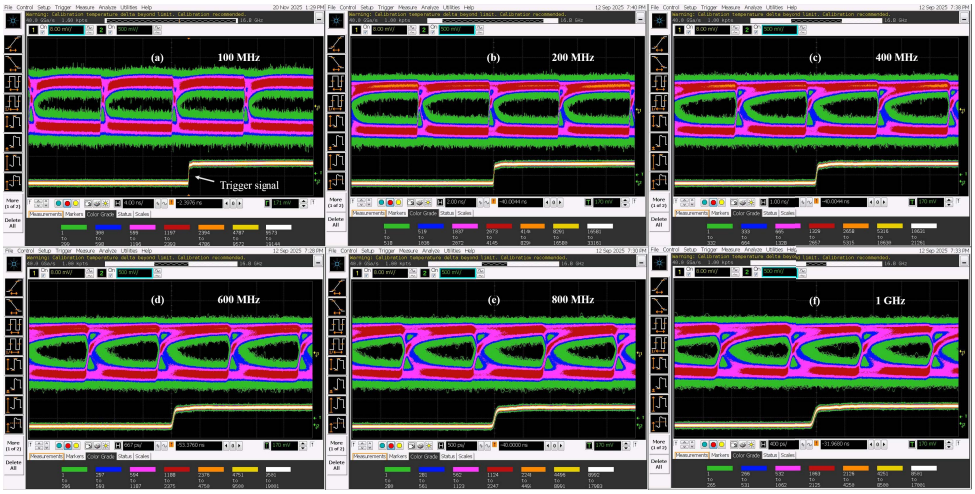



**Fig. 6.** Eye diagrams at different modulation rates. (a)-(f) represent 100 MHz, 200 MHz, 400 MHz, 600 MHz, 800 MHz and 1 GHz respectively. The data were collected using a 16-GHz-bandwidth oscilloscope (DSA-X 91604A) and a 12-GHz-bandwidth photoreceiver (Newport, model 1544-B).

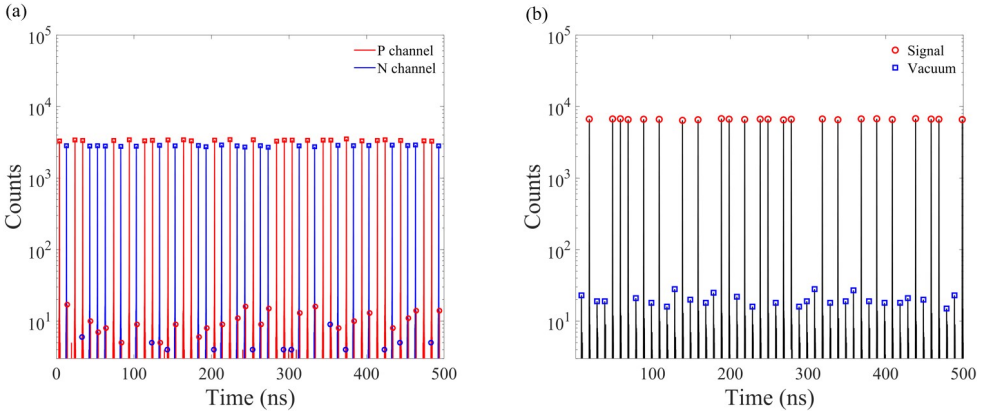



**Fig. 7.** Photon histogram of PN polarization states modulation and decoy state modulation. The modulation rate is 100 MHz. (a) PN polarization states modulation. Red line and blue line represent P channel and N channel respectively. Accordingly, red(blue) squares represent P(N) state in P(N) channel, red(blue) circles represent N(P) state in P(N) channel. (b) Decoy state modulation. Blue squares and red circles represent vacuum and signal states respectively.

## 4. Conclusion and discussion

In this work, we proposed a low-voltage silicon photonics modulator for QKD applications. Through device optimization, the CIM achieved a CMOS-compatible half-wave voltage of 1.28 V at 100 MHz. The modulator exhibits a high modulation depth exceeding 24 dB at this frequency, while maintaining over 21 dB at 1 GHz. These results demonstrate its capability to meet the demanding requirements of QKD systems under low driving voltages. Moreover, the design is fully compatible with standard silicon photonics processes, enabling direct industrial adoption.

Optics EXPRESS

Since the CIM does not require high driving voltages and can be directly driven by CMOS-level signals, it significantly reduces the burden on electronics while lowering power consumption and saving space. This advantage makes our modulator particularly suitable for developing compact, low-power QKD transmitters. The presented work provides a practical solution towards miniaturized QKD terminals, showing great potential for future applications in drones and satellites.

To highlight the significance of our work for integrated QKD system development, we compile several research results on silicon photonic modulator designs in both COC and QKD fields, as summarized in Table 1. As outlined in the Introduction, COC research predominantly prioritizes higher modulator bandwidth, leading to widespread adoption of CDMs. For instance, Ref. [38] demonstrates a silicon photonic modulator achieving 140 GBd operation, albeit with a high half-wave voltage of 54 V that yields merely about 2 dB modulation depth under 5 V driving voltage. While this modulation depth suffices for COC encoding/decoding, QKD systems impose fundamentally different requirements. QKD demands exceptionally high modulation depths (>20 dB typically) to maintain sufficiently low quantum bit error rates (QBER). The inherently low modulation efficiency of CDMs would necessitate prohibitively high driving voltages to meet this requirement. Conversely, the achievable QKD rate is primarily constrained by single-photon detector characteristics including count rate, timing jitter, dead time, and electronic noise. For example, by using high performance SNSPD, Li realized a high-rate QKD system which SKR exceeding 110 Mbps [32]. Although, the timing jitter of their detector is only 60 ps, their modulation rate can only reach 2.5 GHz. This critical distinction suggests that directly integrating COC-optimized CDM designs into QKD systems may be suboptimized. Instead, the CIM, which inherently faces a trade-off between half-wave voltage and bandwidth, emerges as a more suitable solution. While previous work like that of Sax et al. pushed CIM towards high-speed operation [29], our results demonstrate that CIM is particularly advantageous for moderate-speed QKD scenarios. In this regime, the CIM's intrinsic advantage of ultralow driving voltage can be fully leveraged, providing a superior solution for developing compact and efficient QKD transmitters.

**Table 1. Silicon photonics modulators in QKD and COC**

| Ref. | Modulator Type | $V_{pp}/V_{\pi}$ [a] | Modulation Speed | Modulation Depth | Application |
|---|---|---|---|---|---|
| Li [39] | CDM | 3.5 V | 28 GBd | 4.3 dB | COC |
| Xiao [40] | CDM | 6.5 V | 50 GHz | 7.5 dB | COC |
| Yue [38] | CDM | 5 V | 140 GBd | 2.08 dB | COC |
| Sibson [20] | CDM | > 8 V | 1.72 GHz | 20-25 dB | QKD |
| Zhu [25] | CDM | 3.27 V | 312.5 MHz | > 23 dB | QKD |
| Li [32] | CDM | 4.7 V | 2.5 GHz | 22 dB[b] | QKD |
| Nedeljkovic [41] | CIM | 0.25 V (push-pull) | 125 MHz | 22.2 dB (DC) | COC |
| Xu [42] | CIM | 16 V (pre-emphasis) | 12.5 GHz | 9 dB | COC |
| Sax [29] | CIM | 3 V | 2.5 GHz | 20 dB[b] | QKD |
| This work | CIM | 1.1 V | DC | > 24 dB | QKD |
| | CIM | 1.28 V | 100 MHz | > 24 dB | QKD |
| | CIM | 2 V | 1 GHz | > 21 dB | QKD |

[a] $V_{pp}$ (peak-to-peak voltage) is used for COC, $V_{\pi}$ is used for QKD.
[b] These data are calculated using QBER.

Optics EXPRESS

We have also examined several practical aspects of the CIM. Phase-dependent loss (PDL) is inevitable in plasma-dispersion-effect modulators and is present in both CIM and CDM with comparable magnitude. The measured PDL of our CIM is about 1.49 dB/$\pi$, comparable to that of a typical CDM [25,43]. PDL does not affect the half-wave voltage of the modulator, but it can degrade the extinction ratio by introducing an amplitude imbalance between the two arms. Therefore, the PDL of the CIM does not compromise the low-voltage modulation characteristic demonstrated in this work, although it may have a minor effect on the extinction ratio. However, such effects should be taken into account in QKD system implementations, as they may influence the secret key generation performance, with an impact comparable to that of CDM. Regarding the inherent trade-off among device length, bandwidth, and driving voltage, a longer CIM reduces the driving voltage at the cost of lower bandwidth, while a shorter device offers higher bandwidth but requires a higher voltage. Furthermore, longer devices suffer from higher propagation loss and are more sensitive to fabrication imperfections, which can affect yield and uniformity, whereas shorter devices require tighter fabrication tolerances (e.g., in doping profile and lithographic precision). These practical considerations must be taken into account when designing the CIM. For QKD systems operating at relatively low symbol rates (e.g., within 1 GHz), our single long CIM provides a compelling solution. It significantly lowers the driving voltage and simplifies the driver circuitry. For higher-speed QKD systems, a multi-section short-CIM configuration may be preferable [29]. The choice of architecture should therefore be guided by the specific system requirements, with our design being particularly advantageous for practical moderate-speed QKD transmitters.

**Funding.** National Natural Science Foundation of China (12374475); Shanghai Municipal Science and Technology Major Project (2019SHZDZX01); Quantum Science and Techrology-National Science and Technology Major Project (2021ZD0300104, 2021ZD0300108); Natural Science Basis Research Plan in Shaanxi Province of China (2025JC-YBQN-043); Anhui Provincial Natural Science Foundation (2508085J003).

**Disclosures.** The authors declare no conflicts of interest.

**Data availability.** Data underlying the results presented in this paper are not publicly available at this time but may be obtained from the authors upon reasonable request.

## References

1. C. H. Bennett and G. Brassard, "Quantum cryptography: Public key distribution and coin tossing," in *Proceedings of IEEE International Conference on Computers, Systems, and Signal Processing* (IEEE, 1984), p. 175.
2. F. Xu, X. Ma, Q. Zhang, *et al.*, "Secure quantum key distribution with realistic devices," Rev. Mod. Phys. **92**(2), 025002 (2020).
3. C. H. Bennett, F. Bessette, G. Brassard, *et al.*, "Experimental quantum cryptography," J. Cryptology **5**(1), 3–28 (1992).
4. D. Rosenberg, J. W. Harrington, P. R. Rice, *et al.*, "Long-distance decoy-state quantum key distribution in optical fiber," Phys. Rev. Lett. **98**(1), 010503 (2007).
5. T. Schmitt-Manderbach, H. Weier, M. Fürst, *et al.*, "Experimental demonstration of free-space decoy-state quantum key distribution over 144 km," Phys. Rev. Lett. **98**(1), 010504 (2007).
6. H. L. Yin, T. Y. Chen, Z. W. Yu, *et al.*, "Measurement-Device-Independent Quantum Key Distribution over a 404 km Optical Fiber," Phys. Rev. Lett. **117**(19), 190501 (2016).
7. A. Boaron, G. Boso, D. Rusca, *et al.*, "Secure quantum key distribution over 421 km of optical fiber," Phys. Rev. Lett. **121**(19), 190502 (2018).
8. S. Wang, Z.-Q. Yin, D.-Y. He, *et al.*, "Twin-field quantum key distribution over 830-km fibre," Nat. Photonics **16**(2), 154–161 (2022).
9. Y. Liu, W.-J. Zhang, C. Jiang, *et al.*, "1002 km twin-field quantum key distribution with finite-key analysis," Quantum Front. **2**(1), 16 (2023).
10. M. Sasaki, M. Fujiwara, H. Ishizuka, *et al.*, "Field test of quantum key distribution in the Tokyo QKD Network," Opt. Express **19**(11), 10387–10409 (2011).
11. S. Nauerth, F. Moll, M. Rau, *et al.*, "Air-to-ground quantum communication," Nat. Photonics **7**(5), 382–386 (2013).
12. J. Y. Wang, B. Yang, S. K. Liao, *et al.*, "Direct and full-scale experimental verifications towards ground-satellite quantum key distribution," Nat. Photonics **7**(5), 387–393 (2013).
13. Y. L. Tang, H. L. Yin, Q. Zhao, *et al.*, "Measurement-device-independent quantum key distribution over untrustful metropolitan network," Phys. Rev. X **6**(1), 011024 (2016).

Optics EXPRESS


14. S. K. Liao, W. Q. Cai, W. Y. Liu, *et al.*, "Satellite-to-ground quantum key distribution," Nature **549**(7670), 43–47 (2017).
15. J. F. Dynes, A. Wonfor, W. W. Tam, *et al.*, "Cambridge quantum network," npj Quantum Inf. **5**(1), 101 (2019).
16. Y. A. Chen, Q. Zhang, T. Y. Chen, *et al.*, "An integrated space-to-ground quantum communication network over 4,600 kilometres," Nature **589**(7841), 214–219 (2021).
17. Y. Li, W.-Q. Cai, J.-G. Ren, *et al.*, "Microsatellite-based real-time quantum key distribution," Nature **640**(8057), 47–54 (2025).
18. P. Sibson, C. Erven, M. Godfrey, *et al.*, "Chip-based quantum key distribution," Nat. Commun. **8**(1), 13984 (2017).
19. C. Ma, W. D. Sacher, Z. Tang, *et al.*, "Silicon photonic transmitter for polarization-encoded quantum key distribution," Optica **3**(11), 1274 (2016).
20. P. Sibson, J. E. Kennard, S. Stanisic, *et al.*, "Integrated silicon photonics for high-speed quantum key distribution," Optica **4**(2), 172–177 (2017).
21. T. K. Paraïso, I. De Marco, T. Roger, *et al.*, "A modulator-free quantum key distribution transmitter chip," npj Quantum Inf. **5**(1), 42 (2019).
22. G. Zhang, J. Y. Haw, H. Cai, *et al.*, "An integrated silicon photonic chip platform for continuous-variable quantum key distribution," Nat. Photonics **13**(12), 839–842 (2019).
23. H. Semenenko, P. Sibson, A. Hart, *et al.*, "Chip-based measurement-device-independent quantum key distribution," Optica **7**(3), 238–242 (2020).
24. T. K. Paraïso, T. Roger, D. G. Marangon, *et al.*, "A photonic integrated quantum secure communication system," Nat. Photonics **15**(11), 850–856 (2021).
25. C.-X. Zhu, Z.-Y. Chen, Y. Li, *et al.*, "Experimental Quantum Key Distribution with Integrated Silicon Photonics and Electronics," Phys. Rev. Appl. **17**(6), 064034 (2022).
26. Z.-Y. Chen, C.-X. Zhu, Z.-S. Huang, *et al.*, "A 1.25-GHz multi-amplitude modulator driver in 0.18 $\mu$m SiGe BiCOMOS technology for high speed quantum key distribution," Rev. Sci. Instrum. **94**(10), 104703 (2023).
27. D. Bunandar, A. Lentine, C. Lee, *et al.*, "Metropolitan Quantum Key Distribution with Silicon Photonics," Phys. Rev. X **8**(2), 021009 (2018).
28. K. Wei, W. Li, H. Tan, *et al.*, "High-speed measurement-device-independent quantum key distribution with integrated silicon photonics," Phys. Rev. X **10**(3), 031030 (2020).
29. R. Sax, A. Boaron, G. Boso, *et al.*, "High-speed integrated QKD system," Photonics Res. **11**(6), 1007 (2023).
30. L. Cao, W. Luo, Y. X. Wang, *et al.*, "Chip-Based Measurement-Device-Independent Quantum Key Distribution Using Integrated Silicon Photonic Systems," Phys. Rev. Appl. **14**(1), 011001 (2020).
31. M. Avesani, L. Calderaro, M. Schiavon, *et al.*, "Full daylight quantum-key-distribution at 1550 nm enabled by integrated silicon photonics," npj Quantum Inf. **7**(1), 93 (2021).
32. W. Li, L. Zhang, H. Tan, *et al.*, "High-rate quantum key distribution exceeding 110 Mb s-1," Nat. Photonics **17**(5), 416–421 (2023).
33. Q. Xu, B. Schmidt, S. Pradhan, *et al.*, "Micrometre-scale silicon electro-optic modulator," Nature **435**(7040), 325–327 (2005).
34. Z.-Y. Chen, X.-Z. Wang, Y. Li, *et al.*, "Integrated photonics and electronics for high-speed quantum key distribution," Laser Photonics Rev. **20**(3), e01080 (2025).
35. Y. Taur and T. H. Ning, *Fundamentals of Modern VLSI Devices* (Cambridge University Press, 2021), 3rd ed.
36. R. Soref and B. Bennett, "Electrooptical effects in silicon," IEEE J. Quantum Electron. **23**(1), 123–129 (1987).
37. https://compoundtek.com/.
38. H. Yue, J. Fu, H. Zhang, *et al.*, "Silicon modulator exceeding 110 GHz using tunable time-frequency equalization," Optica **12**(2), 203–215 (2025).
39. X. Li, F. Yang, F. Zhong, *et al.*, "Single-drive high-speed lumped depletion-type modulators toward 10 fJ/bit energy consumption," Photonics Res. **5**(2), 134 (2017).
40. X. Xiao, H. Xu, X. Li, *et al.*, "High-speed, low-loss silicon Mach-Zehnder modulators with doping optimization," Opt. Express **21**(4), 4116 (2013).
41. M. Nedeljkovic, C. G. Littlejohns, A. Z. Khokhar, *et al.*, "Silicon-on-insulator free-carrier injection modulators for the mid-infrared," Opt. Lett. **44**(4), 915 (2019).
42. Q. Xu, S. Manipatruni, B. Schmidt, *et al.*, "12.5 Gbit/s carrier-injection-based silicon micro- ring silicon modulators," Opt. Express **15**(2), 430–436 (2007).
43. C. Li, M. Curty, F. Xu, *et al.*, "Secure quantum communication in the presence of phase- and polarization-dependent loss," Phys. Rev. A **98**(4), 042324 (2018).